

Modeling and Tracking Control of Micropipette Oocyte Enucleation Based on Fractional Calculus

Yujie Zhang, Bingxin Li,
Yaowei Liu, *Membership*, and Xin Zhao*, *Membership*

Abstract—The protocol of somatic cell nuclear transfer technology requires oocyte enucleation with a micropipette. This operation is destructive and critical to the further development of reconstructed oocytes. As an aspiration control problem, the viscoelastic property of extracted material, complicated dynamics, great uncertainty, and disturbance bring about difficulties on the subject. To address this issue, this article models the enucleation process with fractional-order calculus. With the same number of parameters, it is shown that the fractional-order models have better fitting performance than integer-order models. In addition, more terms and more parameters can be added to fractional-order models, which strengthens the modeling ability. Based on the identified incommensurate fractional-order model, an adaptive sliding mode controller is proposed to deal with the unknown system parameters and disturbance. In the numerical simulation, the fractional-order controller gets a small overshoot ($< 5\%$) and no oscillation, while the integer-order controller gets a large overshoot ($> 25\%$) and fast oscillation. Experiments on the micromanipulation system compare the fractional-order, integer-order and traditional PID controllers. The results show that the proposed fractional-order controller has shorter arrival time, less arrival velocity, less root mean square error (RMSE), higher success rate and higher cleavage rate. The higher cleavage rate of the proposed fractional-order controller means lower damage to oocytes, which is meaningful for the completion of somatic cell nuclear transfer.

Index Terms—Micromanipulation, Aspiration control, Fractional Order, Adaptive Control, Sliding Mode Control, Somatic Cell Nuclear Transfer.

NOMENCLATURE

$x(t)$	Interface position.
$p(t)$	Decrement of pressure from the balance state.
$r(t)$	Desired trajectory.
$e(t)$	Tracking error.
S	Section area of injection micropipette.

This work was supported in part by the National Natural Science Foundation of China under Grant 62333012 and 62273185. (Corresponding author: Xin Zhao.)

The authors are with the National Key Laboratory of Intelligent Tracking and Forecasting for Infectious Diseases, Engineering Research Center of Trusted Behavior Intelligence, Ministry of Education, Tianjin Key Laboratory of Intelligent Robotics (tikLIR), Institute of Robotics and Automatic Information System (IRAIS), Nankai University, Tianjin 300350, China, and also with the Institute of Intelligence Technology and Robotic Systems, Shenzhen Research Institute of Nankai University, Shenzhen 518083, China (e-mail: zhaoxin@nankai.edu.cn).

${}^C\mathcal{D}^\alpha, \mathcal{D}^\alpha$	Caputo definition of fractional order derivative.
${}_{t_0}^{RL}\mathcal{D}^\alpha, {}_{t_0}^{GL}\mathcal{D}^\alpha$	Riemann-Liouville and Grünwald-Letnikov definitions of fractional order derivative.
α_i, β_i	Fractional orders, $\beta_i = \alpha_i + \alpha_{i-1}$.
$\bar{\alpha}$	Vector of fractional orders.
$\hat{\theta}$	Estimation of θ .
θ	System parameter.
a_m, d_m	Maximum acceleration and deceleration.
b	Gain of system input.
$d(t)$	System disturbance and uncertainty.
k, l, Γ, K	Controller gains.
M, α	Controller parameters.
n	System order.
P, Q, E, ψ	Matrix variables of the controller.
u_m, u_M	Minimum and maximum of control input.
v_m	Maximum speed.
x_f, t_f	Desired final position and arrival time.

I. INTRODUCTION

SINCE the first cloned mammal Dolly [1] was created, the somatic cell nuclear transfer (SCNT) technology has been influencing the animal breeding and biological research. Faced with the challenge of resource shortage and increasing demand for animal products, people use SCNT technology to increase the global output of livestock products [2]. Many countries have applied the SCNT technology to commercial livestock reproduction and preservation [3]. SCNT technology can also be combined with other recently developed technologies. For example, SCNT can provide embryonic stem cells (ESCs) for clinical usage or biological research [4]. After transgenesis, SCNT can generate animals from genetically modified cells [5]. Compared to induced pluripotent stem cells (iPSCs), SCNT shows fewer epigenetic and transcriptomic aberrations [6], thus better stem cells can be provided. Animal cloning for pigs provides good models for human medical research, as well as good donors for organ transplantation into humans. The success of SCNT in monkeys fills a need for non-human primate models [7], which could pave the way for tackling brain diseases [8].

However, the broad usage of SCNT remains limited due to its high cost and low efficiency in obtaining live and healthy offspring [5]. SCNT technology mainly involves the enucleation of oocytes and the injection of somatic cells. Over

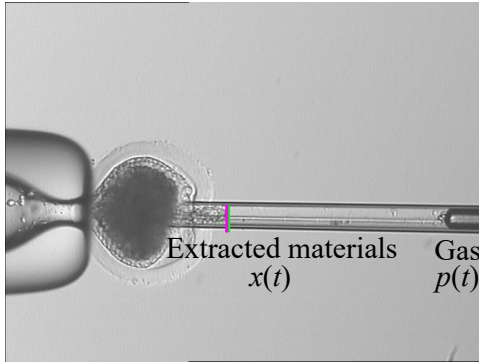


Fig. 1. Microscopic image of enucleation process. By adjusting the gas pressure $p(t)$, the interface position of extracted material $x(t)$ changes.

the past few years, robotic systems have been developed to improve the efficiency [9]. The rotation force [10], oocyte orientation [11] and penetration speed [12] have been optimized. These are open-loop optimizations.

So far, the most common nuclear transfer protocol involves glass pipettes for enucleation and injection [5]. The enucleation operation needs to tear the genetic material and part of the cytoplasm apart from the oocyte, which is the most difficult and destructive step in the SCNT procedure. To realize smooth enucleation and reduce the damage to the recipient oocyte, the enucleation process must be better modeled and accurately controlled.

During the enucleation process, some material in the oocyte is aspirated into the micropipette (**Fig. 1**), which can be considered as an aspiration control problem. Existing aspiration and positioning methods [13]–[17] deal with cells as a whole, or consider the cells as elastic solid matters. These methods model the controlled systems as modified mass-spring-damper systems, where the mass and damping coefficient may vary during the process. However, the extracted oocyte material in the enucleation process is a kind of viscoelastic material and exhibits more fluid properties [18].

The mass-spring-damper system can be formulated as second-order differential equations and there are generally 3 equivalent system parameters. When the orders are not constrained to integers, non-integer-order differential models can be obtained and more parameters can be added. Such models are known as ‘fractional’ order models. Fractional-order derivative has a firm and long-standing theoretical foundation [19] [20] and has been successfully used in several systems analytically or practically [21], including blood flow [22], smart material [23], dielectric elastomer actuators [24] and multiagent systems [25]. It has superiority in modeling many complex materials. Cells and other biomaterials are distributed-parameter systems that exhibit viscoelasticity, creep, stress relaxation and memory property [26]. A 0.5-order differential relationship between strain and stress was obtained for a viscoelastic material [27]. It was observed that fractional-order differentiation could fit better with empirical results of such systems with viscoelasticity and memory property [24] since these structures are essentially distributed-parameter systems. In addition, the corresponding models have

the advantage in linear viscoelasticity in that fewer parameters are required while better performance can be achieved [28]. Efficient control of micropipette-based oocyte enucleation is intractable mainly because of the complex characteristics of intracellular materials. The materials show viscosity and elasticity. In the experiments, the extracted materials often shrink to a sphere under the interfacial tension [29]. The integer-order spring-damper model is not accurate enough to model such material, while the fractional-order model can better describe the viscoelasticity and distributed interfacial tension. In addition, the mass can be disregarded in this process because the gravity is much less than gas pressure variation. So, the integer-order spring-damper model is inappropriate to describe the enucleation process. However, due to the unintuitive characteristic and numerical complexity, the usage of fractional-order models and controllers is still limited [19]. The fractional-order sliding mode controllers have been designed for linear motors [30] and quadcopters [31] [32]. These systems are essentially integer-order systems. To the best of the author’s knowledge, most of the previously applied controllers were designed for commensurate fractional-order systems where the orders are the same, or the models were approximated to integer-order models [24]. Few studies have applied the incommensurate fractional-order model in practice [33] [34] and some of them restrict the orders of the system model where the orders $\alpha_i = 1(1 \leq i \leq n - 1)$. The application of incommensurate fractional-order models is still limited.

A challenge in enucleation control is complex dynamics, high diversity, great uncertainty and disturbance. Cell inner pressure [35], capillary force [36], and the viscosity of oocytes and culture medium [17] all influence the enucleation process. These parameters vary among different experiments. Additionally, micropipettes may be blocked by contaminants. The major advantage of sliding mode control is low sensitivity to plant parameter uncertainties and disturbances, which are significant during the enucleation operation.

Considering the above, this article first identifies fractional-order models of the pneumatic enucleation process based on experimental data, and the fractional-order models are compared with integer-order models of the same number of parameters, indicating the superiority of the fractional-order model. Secondly, these fractional-order models are unified and formulated into a multivariable linear fractional-order model with unknown parameters and disturbance. Furthermore, a fractional-order adaptive sliding mode controller (FOASMC) is designed to deal with unknown parameters and system disturbance. Finally, simulations and experiments are performed to validate the fractional-order controller. Compared with the existing studies, the contributions of this article are summarized as follows:

- 1) The oocyte enucleation process was modeled with fractional-order differentiation, which is able to capture the viscoelastic behavior with fewer parameters and better performance. Results of fitting with integer- and fractional-order differentiation demonstrate the superiority of fractional-order models.
- 2) An adaptive sliding mode controller was designed for

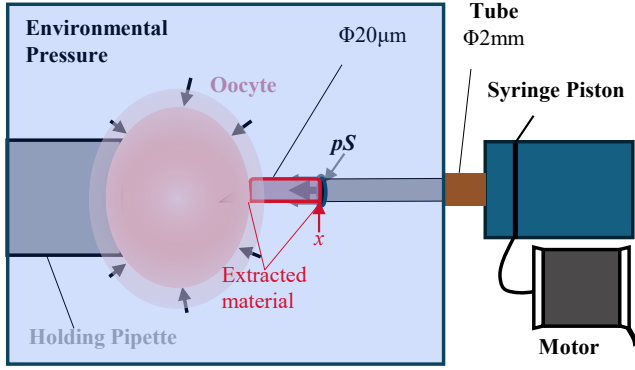


Fig. 2. The illustration of micropipette oocyte enucleation process.

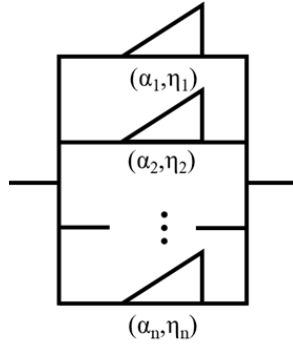


Fig. 3. The fractional Kelvin-Voigt-like model.

the incommensurate fractional-order system, where the fractional orders are different. The stability of the controlled system is proven. Simulations demonstrate the superiority of fractional-order controllers over integer-order controllers. Experiments on porcine oocytes validate the proposed controller.

The rest of this article is organized as follows. Section II numerically models the overall dynamics of oocyte enucleation and formulates the control problem. The fractional-order models are compared with integer-order models. Section III gives the controller design and the proof of stability. In Section IV, the model is validated by simulations and experimental results. At last, Section V concludes this article.

II. SYSTEM MODEL

The configuration of the micropipette-based oocyte enucleation system is depicted in **Fig. 2**. The oocyte is fixed by the holding micropipette and penetrated by another thinner micropipette ($20\mu\text{m}$). The pipettes are connected to pneumatic pumps which are driven by motors. The motors communicate with an industrial personal computer (IPC) through self-developed software. During the oocyte enucleation process, the pressure in the micropipette is adjusted by moving the syringe piston which is connected to a motor. When the pressure in the micropipette decreases, the pressure in the environment squeezes the cytoplasm out of the oocyte. When the amount in the micropipette is sufficient to remove the genetic material in the oocyte, i.e. the interface position x arrives at the target

position, the micropipette withdraws from the oocyte and the enucleation process is completed.

If the extracted material is considered as elastic solid material, the displacement is proportional to the external force. The constitutive relation is formulated as:

$$x(t) \propto p(t)S, \quad (1)$$

where $x(t)$ is the interface position, $p(t)$ is the decrement of pressure from the balance state and S is the section area. If the material is considered as viscous fluid, the velocity is proportional to the external force. The constitutive relation is:

$$\dot{x}(t) \propto p(t)S, \quad (2)$$

Note that the stress is proportional to the zeroth derivative of strain for elastic material and to the first derivative of strain for viscous material. For the viscoelastic material, it is natural to suppose that the stress is proportional to the strain of the order between zero and one [37], which was analyzed with molecular theory [28]. Here we use the definition of Caputo [38] for fractional-order differentiation:

$${}_{t_0}\mathcal{D}_t^\alpha f(t) = \frac{1}{\Gamma(m-\alpha)} \int_{t_0}^t \frac{f^{(m)}(\tau)}{(t-\tau)^{1+\alpha-m}} d\tau, \quad (3)$$

where α is the order of differentiation, $m-1 < \alpha < m$, $\alpha \in \mathbb{R}$, $m \in \mathbb{Z}^+$, $\Gamma(s) = \int_0^\infty t^{s-1} e^{-t} dt$. ${}_{t_0}\mathcal{D}_t^\alpha[\cdot]$ is the symbol of fractional-order differentiation. Because t_0 is considered to be zero by default, t_0 and t are omitted in the following context. The constitutive relation of fractional viscoelastic element is:

$$\mathcal{D}^\alpha x(t) \propto p(t)S. \quad (4)$$

Considering the fractional-order Kelvin–Voigt model [39] that is depicted in **Fig. 3**, the constitutive relation is:

$$\sum_{i=1}^n \eta_i \mathcal{D}^{\alpha_i} x(t) = p(t)S. \quad (5)$$

Where η_i s and α_i s are element parameters. The interface is stationary before the operation, i.e. $x(t) = 0, \forall t \leq 0$. There are different types of injection systems, and $p(t)$ is approximately linear to the position of syringe piston. Therefore, we regard $p(t)$ as control input and $x(t)$ as output. To test the superiority of fractional-order models over integer-order models, several experiments were performed to collect data.

Considering (5), the relationship of $p(t)$ and $x(t)$ can be formulated as $\frac{X(s)}{P(s)} = G(s)$, where $X(s)$ and $P(s)$ are Laplace transform of $x(t)$ and $p(t)$, $G(s)$ is a rational fraction of s . Previously, the denominator of $G(s)$ was considered as a quadratic polynomial. But fractional-order differentiation allows deviation from the quadratic polynomial. A small deviation is added to the orders to get a fractional-order model and keep the number of tunable parameters the same. The following form of integer-order and fractional-order transfer functions $G_{io-2}(s)$ and $G_{fo-2}(s)$ are considered:

$$\begin{aligned} G_{io-2}(s) &= \frac{1}{a_{i2}s^2 + a_{i1}s + a_{i0}}, \\ G_{fo-2}(s) &= \frac{1}{a_{f2}s^{2.2} + a_{f1}s^{1.1} + a_{f0}}, \end{aligned} \quad (6)$$

where $a_{ik}, a_{fk} (k = 0, 1, 2)$ are constant coefficients to be determined. Given the transfer functions and control input $p(t)$, the simulated output of $G_{io-2}(s)$ and $G_{fo-2}(s)$ are defined as [40]:

$$\begin{aligned} x_{io-2}(t_i) &= \frac{p_i - \sum_{k=0}^2 \frac{a_{ik}}{h^k} \sum_{j=1}^i w_j^{(k)} x_{io-2}(t_{i-j})}{\sum_{k=0}^2 \frac{a_{ik}}{h^k}} \\ x_{fo-2}(t_i) &= \frac{p_i - \sum_{k=0}^2 \frac{a_{fk}}{h^{1.1k}} \sum_{j=1}^i w_j^{(1.1k)} x_{fo-2}(t_{i-j})}{\sum_{k=0}^2 \frac{a_{fk}}{h^{1.1k}}} \end{aligned} \quad (7)$$

where $t_{i+1} - t_i = h$, h is the step size, p_i is the sampled value of pressure at t_i . $w_j^{(\alpha)}$ can be evaluated recursively:

$$w_0^{(\alpha)} = 1, \quad w_j^{(\alpha)} = \left(1 - \frac{\alpha + 1}{j}\right) w_{j-1}^{(\alpha)}, j = 1, 2, \dots \quad (8)$$

Remark 1. Equation (7) uses the definition of Grünwald-Letnikov fractional derivative. For a wide class of functions which appear in real physical and engineering applications, Riemann-Liouville and Grünwald-Letnikov definitions of fractional order derivative are equivalent [20]. The relationship of Caputo and Riemann-Liouville derivative [41] is

$${}^C_{t_0} \mathcal{D}^\alpha x(t) = {}^{RL}_{t_0} \mathcal{D}^\alpha x(t) - \sum_{j=0}^{n-1} \frac{x^{(j)}(t_0) (t - t_0)^{j-\alpha}}{\Gamma(j - \alpha + 1)},$$

where $n = [\alpha] + 1$. Because the inner material of oocyte keeps static before the operation, the initial condition of system output $x(t)$ is $x^{(j)}(t_0) = 0, j = 0, 1, \dots, n-1$. Therefore, the second term in the right side of the equation above is 0. Thus,

$${}^C_{t_0} \mathcal{D}^\alpha x(t) = {}^{RL}_{t_0} \mathcal{D}^\alpha x(t) = {}^{GL}_{t_0} \mathcal{D}^\alpha x(t).$$

where ${}^C_{t_0} \mathcal{D}^\alpha$, ${}^{RL}_{t_0} \mathcal{D}^\alpha$ and ${}^{GL}_{t_0} \mathcal{D}^\alpha$ are Caputo, Riemann-Liouville and Grünwald-Letnikov definitions of fractional order derivative respectively.

Based on the data obtained from enucleation experiments, optimal $G_{io-2}(s)$ and $G_{fo-2}(s)$ are searched out with prescribed constraints. The optimal value \mathbf{a}_{io-2}^* and \mathbf{a}_{fo-2}^* are defined in the sense of least mean square:

$$\begin{aligned} \mathbf{a}_{io-2}^* &= \operatorname{argmin}_{\mathbf{a}_{io-2}} \sum_{i=0}^n (x_{io-2}(t_i) - x_i)^2, \\ \mathbf{a}_{fo-2}^* &= \operatorname{argmin}_{\mathbf{a}_{fo-2}} \sum_{i=0}^n (x_{fo-2}(t_i) - x_i)^2, \end{aligned} \quad (9)$$

where x_i is the sampled value of interface position at t_i . $\mathbf{a}_{io-2} = (a_{i0}, a_{i1}, a_{i2})$, $\mathbf{a}_{fo-2} = (a_{f0}, a_{f1}, a_{f2})$ and the corresponding transfer functions are $G_{io-2}^*(s)$ and $G_{fo-2}^*(s)$.

With the same initial guess of parameters, the trust region reflective algorithm solves \mathbf{a}_{io-2}^* and \mathbf{a}_{fo-2}^* . The simulated response to $p(t)$ of $G_{io-2}^*(s)$ and $G_{fo-2}^*(s)$ are plotted in Fig. 4 for example. It is observed that the fractional-order model has a smaller error.

Moreover, infinite items of orders below a certain number can be added, which strengthens the modeling ability, while avoiding introducing large noises. We further demonstrate that the fractional orders can also be adjusted and optimized,

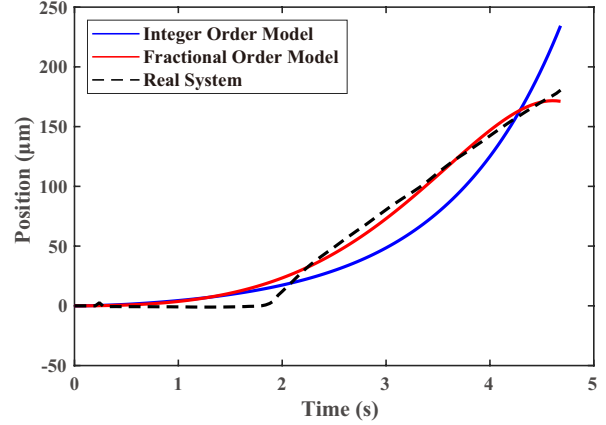


Fig. 4. Identified integer-order model output (blue), fractional-order model output (red) and experimental data (dashed) of group 5. The fractional-order model has a smaller error.

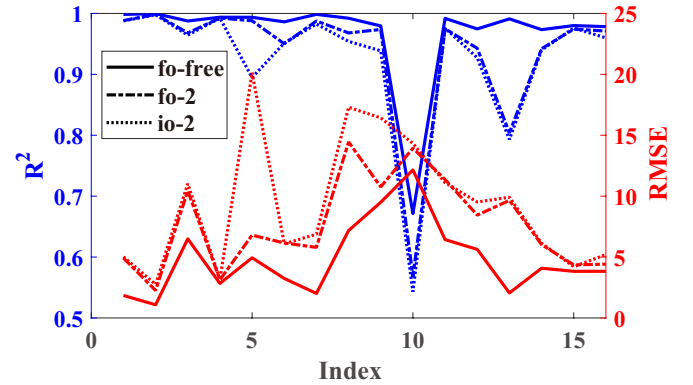


Fig. 5. Comparison of identification results with different models. Solid line: fo-free; dash-dotted line: fo-2; dotted line: io-2. The x-axis represents the index of different data groups. Blue lines are the R-square values and the red lines are the RMSE values.

producing better results. $G_{fo-free}(s)$ is constrained in the following form:

$$G_{fo-free}(s) = \frac{1}{a_3 s^{\beta_3} + a_2 s^{\beta_2} + a_1 s^{\beta_1} + a_0 s^{\beta_0}}. \quad (10)$$

where $\beta_i \in [0, 3.5], i = 0, 1, 2, 3$. The MATLAB toolkit FOMCON [42] provides a tool to identify the fractional-order transfer function based on time-domain data. Using the Grünwald-Letnikov method and trust-region-reflective algorithm [43], all identified orders are rational due to the digital computation. The results are compared with 3-parameter integer-order (io-2) and fractional-order (fo-2) models in Fig. 5. For example, the identified model of group 2 is

$$G_{fo-free}^*(s) = \frac{1}{7.08s^{2.78} - 5.07s^{2.42} + 2.44s^{1.34} - 0.24s^{0.36}} \quad (11)$$

Remark 2. From Fig. 5, the average R^2 value of identified fractional-order models (0.9370) is greater than that

of the integer-order models (0.9237), and the average root mean square error (RMSE) value of identified fractional-order models (7.6827) is smaller than that of integer-order models (9.3260), indicating the fractional-order models fit the enucleation process more accurately. This is attributed to its superiority in the modeling of viscoelasticity and memory behavior. This model works like a fuzzy system or a neural network, with its nature that can describe the viscoelasticity well. A little variation of the fractional orders has little impact on the whole system. The identified fractional-order model of the group 2 is set as the system model in the simulation due to its minimum RMSE value. The models are **incommensurate**, which means $\beta_i = \lambda_i \beta_0, i > 0, \lambda_i \in \mathbb{Z}^+$ does not hold. The usual stability analysis of incommensurate fractional-order systems involves the complicated LMI. And it is time-consuming to solve the LMIs in the application. To the author's knowledge, there are few applications of the incommensurate fractional order models. Many works focus on the stability analysis of such systems. The design of sliding mode control for high-order fractional-order systems is lacking.

Let $x_1(t) = x(t)$ denote the current position of the interface. Taking the matched and unmatched disturbance into account, system (5) can be reformulated as:

$$\begin{cases} \mathcal{D}^{\alpha_i} x_i(t) &= x_{i+1}(t), i = 1, 2, \dots, n-1 \\ \mathcal{D}^{\alpha_n} x_n(t) &= \theta^T \mathbf{x}(t) + bu(t) + d(t) \\ y(t) &= x_1(t), \end{cases} \quad (12)$$

where n is the system order, $x_i(t), i = 1, 2, \dots, n$ are state variables, $\mathbf{x}(t) = [x_1(t), x_2(t), \dots, x_n(t)]^T$, $\alpha_i, i = 1, 2, \dots, n$ are fractional orders, $u(t)$ is the system control input, which is a scale, $d(t)$ is the matched and unmatched disturbance, $y(t)$ is the system output, which is also a scale and should follow a designed trajectory $r(t)$. $\theta = [\theta_1, \theta_2, \dots, \theta_n]^T$ is the system parameter. $0 < \alpha_i < 1, i = 1, 2, \dots, n$, and the following assumptions hold: $b > 0$, so that the positive $u(t)$ causes the increment of $x(t)$. The disturbance $d(t)$ is bounded, i.e. $\exists M < +\infty, \forall t, |d(t)| < M$.

III. CONTROLLER DESIGN

In order to design a proper controller for the incommensurate fractional-order system and prove the stability, two lemmas are provided.

Lemma 1 [44] For an incommensurate fractional-order system $\mathcal{D}^{\bar{\alpha}} \mathbf{x}(t) = A \mathbf{x}(t)$, The zero point of this system is Lyapunov globally asymptotically stable if all the roots λ s of the equation

$$\begin{vmatrix} \lambda^{m\alpha_1} - a_{11} & -a_{12} & \dots & -a_{1n} \\ -a_{21} & \lambda^{m\alpha_2} - a_{22} & \dots & -a_{2n} \\ \vdots & \vdots & \ddots & \vdots \\ -a_{n1} & -a_{n2} & \dots & \lambda^{m\alpha_n} - a_{nn} \end{vmatrix} = 0 \quad (13)$$

satisfies $|\arg(\lambda)| > \pi/2m$, where $\bar{\alpha} = [\alpha_1, \alpha_2, \dots, \alpha_n]^T$, $\mathcal{D}^{\bar{\alpha}} \mathbf{x}(t) = [\mathcal{D}^{\alpha_1} x_1(t), \mathcal{D}^{\alpha_2} x_2(t), \dots, \mathcal{D}^{\alpha_n} x_n(t)]^T$, $A = (a_{ij})_{n \times n}$, m is the least common multiple of denominators u_i s of α_i s, $\alpha_i = v_i/u_i, (u_i, v_i) = 1, u_i, v_i \in \mathbb{Z}^+, i = 1, \dots, n$. **Lemma 2** For a given vector function $\mathbf{v}(t) = [v_1(t), \dots, v_n(t)]^T$ such that $\lim_{t \rightarrow +\infty} \|\mathbf{v}(t)\| = 0$,

and state vector $\mathbf{x} = [x_1, \dots, x_n]^T$ which varies as $\mathcal{D}^{\bar{\alpha}} \mathbf{x}(t) = A \mathbf{x}(t) + \dot{\mathbf{v}}(t)$. If A and $\bar{\alpha}$ satisfy stable condition in **Lemma 1**, then $\lim_{t \rightarrow +\infty} x_i(t) = 0, i = 1, \dots, n$. See the proof in the Appendix.

A. Fractional Order Adaptive Sliding Mode Controller

Given a desired trajectory $r(t)$, and let tracking error be $e_1(t) = e(t) = r(t) - y(t)$, denote with $e_{i+1} = \mathcal{D}^{\alpha_i} e_i(t), i = 1, 2, \dots, n$, $\mathbf{e}(t) = [e_1(t), e_2(t), \dots, e_n(t)]^T$, $\beta_0 = 0, \beta_k = \sum_{i=1}^k \alpha_i = \beta_{k-1} + \alpha_k, k = 1, 2, \dots, n$, the dynamics of error e_i s can be obtained as follows:

$$\mathcal{D}^{\alpha_i} e_i(t) = e_{i+1}, i = 1, 2, \dots, n-1. \quad (14)$$

Using (12), we can get

$$\begin{aligned} \mathcal{D}^{\alpha_n} e_n(t) &= \mathcal{D}^{\beta_n} r(t) - \mathcal{D}^{\beta_n} x(t) \\ &= \mathcal{D}^{\beta_n} r(t) - \mathcal{D}^{\alpha_n} x_n(t) \\ &= \mathcal{D}^{\beta_n} r(t) - \theta^T \mathbf{x}(t) - bu(t) - d(t). \end{aligned} \quad (15)$$

It is assumed that the designed trajectory satisfies that all $\mathcal{D}^{\beta_i} r(t)$ s are bounded, i.e. $\mathcal{D}^{\beta_i} r(t) \in L_\infty$. With **Lemma 1**, we hope to obtain

$$\mathcal{D}^{\bar{\alpha}} \mathbf{e}(t) = A_e \mathbf{e}(t), \quad (16)$$

where A_e satisfies the stable condition, such that the tracking error $\mathbf{e}(t)$ converge to zero. Considering equation (14), A_e is like

$$A_e = \begin{bmatrix} 0 & 1 & 0 & \dots & 0 \\ 0 & 0 & 1 & \dots & \vdots \\ \vdots & \vdots & \ddots & \ddots & 0 \\ 0 & 0 & \dots & 0 & 1 \\ -k_1 & -k_2 & -k_3 & \dots & -k_n \end{bmatrix}, \quad (17)$$

where k_i s are to be determined. Denote with $K = [k_1, \dots, k_n]^T$, equation (16) and (17) indicates that system input should make $\mathcal{D}^{\alpha_n} e_n(t) = -\sum_{i=1}^n k_i e_i(t) = -K^T \mathbf{e}(t)$.

We thus design the sliding mode surface as

$$s(t) = \int_0^t (K^T \mathbf{e}(t) + \mathcal{D}^{\alpha_n} e_n(t)) dt. \quad (18)$$

When $\dot{s}(t) = 0$, we get $u_{eq}(t) = \frac{1}{b}(K^T \mathbf{e}(t) + \mathcal{D}^{\beta_n} r(t) - \theta^T \mathbf{x}(t) - d(t))$. Considering the parameter uncertainty, we design the control input as follows.

$$\begin{aligned} u(t) &= \frac{1}{b}(K^T \mathbf{e}(t) + \mathcal{D}^{\beta_n} r(t) - \hat{\theta}^T(t) \mathbf{x}(t) \\ &\quad + ks(t) + \text{sgn}(s(t))M), \\ \hat{\theta}(t) &= \theta - \tilde{\theta}(t), \\ \dot{\tilde{\theta}} &= \Gamma(\mathbf{x}s - \alpha \frac{PE^T}{\|E\|}). \end{aligned} \quad (19)$$

where P and E are defined with

$$\begin{aligned} \dot{P} &= -lP + \mathbf{x}\mathbf{x}^T, P(0) = 0, \\ \dot{Q} &= -lQ + \mathbf{x}(\mathcal{D}^{\beta_n} r(t) + K^T \mathbf{e}(t) - bu(t) - \dot{s})^T, Q(0) = 0, \\ E &= \hat{\theta}^T P - Q = -\tilde{\theta}^T P + \psi, \\ \psi &= -\int e^{-l(t-\tau)} d(\tau) \mathbf{x}^T(\tau) d\tau. \end{aligned} \quad (20)$$

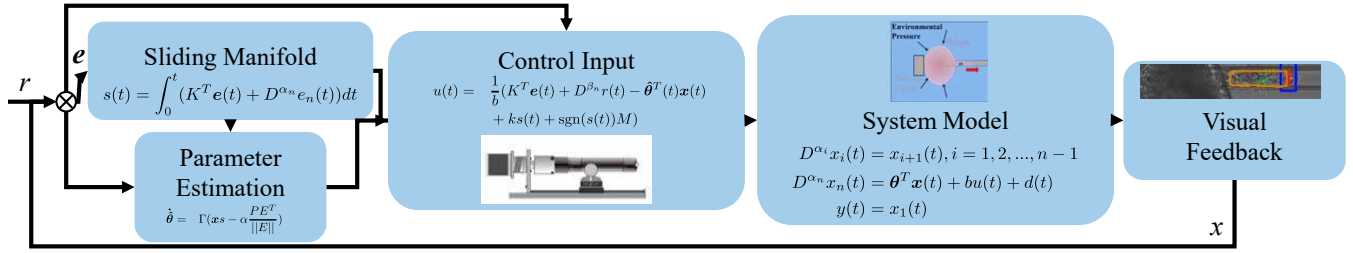


Fig. 6. Block diagram of the system.

$\hat{\theta}(t)$ is the estimate of θ , $\tilde{\theta}(t)$ is the estimation error, Γ is a symmetric positive definite matrix, k, α and l are positive constants. The block diagram of the system is shown in Fig. 6.

B. Stability Analysis

Let the Lyapunov function be

$$V = \frac{1}{2}s^2 + \frac{1}{2}EP^{-1}\Gamma^{-1}P^{-1}E^T, \quad (21)$$

then

$$\begin{aligned} \dot{V} &= s\dot{s} + EP^{-1}\Gamma^{-1}(P^{-1}\dot{E}^T) \\ &= s(\mathcal{D}^{\beta_n}r + K^T e - \theta^T x - d - (\mathcal{D}^{\beta_n}r + K^T e - \hat{\theta}^T x \\ &\quad + ks + M\text{sgn}(s))) + EP^{-1}\Gamma^{-1}(P^{-1}\dot{E}^T) \\ &= -ks^2 - M|s| - ds - \tilde{\theta}^T x s \\ &\quad + EP^{-1}\Gamma^{-1}(\dot{\theta} + (P^{-1}\dot{\psi}^T)) \\ &= -ks^2 - M|s| - ds - \tilde{\theta}^T x s \\ &\quad + EP^{-1}(xs - \alpha \frac{PE^T}{\|E\|} + \Gamma^{-1}\xi) \\ &= -ks^2 - M|s| - ds + \psi P^{-1}xs - \alpha \|E\| \\ &\quad + EP^{-1}\Gamma^{-1}\xi \\ &\leq -(M - |d| - |\psi| \cdot \|P^{-1}\| \cdot \|x\|)|s| \\ &\quad - (\alpha - \|P^{-1}\| \cdot \|\Gamma^{-1}\| \cdot \|\xi\|)\|E\|, \end{aligned} \quad (22)$$

where $\xi = (P^{-1}\dot{\psi}^T)$. It can be proved that there exist $\hbar, \sigma, \delta, T > 0$ such that for each $t > T$, the following inequalities hold [45]:

$$\begin{aligned} |d| &\leq d_M, & |\psi| &\leq \hbar, \\ P &\geq \sigma I, & \|\xi\| &\leq \delta. \end{aligned}$$

Therefore,

$$\begin{aligned} \dot{V} &\leq -(M - |d| - |\psi| \cdot \|P^{-1}\| \cdot \|x\|)|s| - \\ &\quad (\alpha - \|P^{-1}\| \cdot \|\Gamma^{-1}\| \cdot \|\xi\|)\|E\| \\ &\leq -(M - d_M - \frac{\hbar\|x\|}{\sigma})|s| - (\alpha - \frac{\delta\lambda_{max}(\Gamma^{-1})}{\sigma})\|E\|. \end{aligned} \quad (23)$$

Choose M, α such that

$$\begin{aligned} M - d_M - \frac{\hbar\|x\|}{\sigma} &\geq 0, \\ \alpha - \frac{\delta\lambda_{max}(\Gamma^{-1})}{\sigma} &\geq 0. \end{aligned} \quad (24)$$

Then

$$\dot{V} \leq -a\sqrt{V}, \quad (25)$$

where

$$\begin{aligned} a &= 2 \min\{M - d_M - \frac{\hbar\|x\|}{\sigma}, \\ &\quad \sigma^2(\alpha - \frac{\delta\lambda_{max}(\Gamma^{-1})}{\sigma})/\lambda_{max}(\Gamma^{-1})\}. \end{aligned} \quad (26)$$

Add we can get V converges to zero in finite time, so s converges to zero in finite time. Using Lemma 1, we can get the error e globally asymptotically converges to zero.

Remark 3. The adaption law can be simplified as $\dot{\hat{\theta}} = \Gamma xs$. Let the Lyapunov function be $V_2(t) = \frac{1}{2}s^2(t) + \frac{1}{2}\tilde{\theta}^T(t)\Gamma^{-1}\tilde{\theta}(t)$, we can get $\dot{V}_2(t) \leq -ks^2(t) \leq 0$. So, $\dot{V}(t)$ is semi-negative definite, which implies $V(t) \leq V(0)$, $s(t)$ and $\tilde{\theta}(t)$ are bounded. Also, $\dot{V}(t) = 0 \implies s(t) = 0$. According to LaSalle's principle, we have $\lim_{t \rightarrow +\infty} s(t) = 0$. By using Lemma 2, we get $\lim_{t \rightarrow +\infty} e_i(t) = 0, i = 1, \dots, n$, so $e_i(t)s$ are bounded. In addition,

$$\begin{aligned} \mathcal{D}^{\beta_i}r(t), s(t), \tilde{\theta}(t), e_i(t) \in L_\infty &\implies x_i(t), \hat{\theta}(t) \in L_\infty \\ &\implies u(t) \in L_\infty. \end{aligned} \quad (27)$$

Thus the designed controller is globally asymptotically stable, and all the signals in the loop are bounded.

IV. SIMULATIONS AND EXPERIMENTS

A. Simulations

To validate the proposed controller and protect the equipment from possible damage, simulations on MATLAB/Simulink are performed.

The desired trajectory is set as a function that accelerates at the highest acceleration a_m at first, then travels at constant speed v_m , and finally decelerates at the maximum deceleration d_m to 0. At the same time, it travels from 0 to x_f at t_f . In the real system, the input $u(t)$ is limited because motors have boundary positions and maximum speed. We add this constraint in the simulation as well for comparison, which is formulated as $u_m \leq u(t) \leq u_M$. The disturbance is set as $d(t) = 1.5 \sin(t)$, and the upper bound is set as $M = 2$.

The controlled system is set as (11). Four controllers (IOASMC-2, FOASMC-2, FOASMC-custom, CFOASMC-custom) are adopted to control the system. In practice, the exact orders of real systems vary in different experiments. Therefore, the prescribed orders are set different from the

controlled system. For the integer-order adaptive sliding mode controller IOASMC-2, prescribed orders are $\hat{\alpha}_{io-2} = [1, 1]$. For the FOASMC-2, prescribed orders are $\hat{\alpha}_{fo-2} = [1.1, 1.1]$. For the FOASMC-custom, the orders are $\hat{\alpha}_{fo-custom} = [0.4, 0.8, 0.6, 0.4, 0.6]$. The trajectory parameters, model parameters and controller parameters are listed in TABLE I. For constrained FOASMC-custom (CFOASMC-custom), $u_M = 300$ and $u_m = -300$. For other three controllers, there are no constraints on $u(t)$.

Remark 4. Except for the orders, all the tunable parameters of IOASMC-2 and FOASMC-2 are the same.

TABLE I
PARAMETERS OF TRAJECTORY, MODEL AND CONTROLLERS

Symbol	Value	Symbol	Value
a_m	20	α	10
d_m	20	M	2
v_m	30	u_M	300
x_f	80	u_m	-300
t_f	5	$d(t)$	$1.5 \sin(t)$
k	10	n	5
l	1	b	0.1412
Symbol	Value		
$\hat{\alpha}^T$	[0.36, 0.98, 0.66, 0.42, 0.36]		
θ^T	[0, 0.0339, -0.3446, 0, 0.7161]		
$\hat{\alpha}^T$	[1, 1](io-2), [1.1, 1.1](fo-2) [0.4, 0.8, 0.6, 0.4, 0.6](fo-custom)		
$\hat{\theta}^T(0)$	[1, 1] (io-2, fo-2) [1, 1, 1, 1, 1] (fo-custom)		
K^T	[2, 2] (io-2, fo-2) [2, 10, 20, 10, 10](fo-custom)		
Γ	diag([0.001, 0.001]) (io-2, fo-2) diag([0.001, 0.001, 0.0001, 0.0001, 0.0001])		

In the identification step, the parameter b is also supposed to be optimized, which means it is unknown. But for the enucleation system, when $u(t)$ is positive, state variable $x(t)$ never decelerates, which indicates $b \geq 0$. If $b = 0$, the term is omitted. Therefore, $b > 0$ is guaranteed. The value of b can also be estimated according to the system dynamics. In the following simulations, b is unknown and is estimated as $\hat{b} = 1$. Due to the good modeling ability of the fractional-order model with multiple terms, it is supposed to be able to approximate the controlled system locally.

For the IOASMC-2, simulation results of the real trajectory $x(t)$ and the target trajectory $r(t)$ are plotted in Fig. 7. The overshoot is large ($> 25\%$) and the trajectory oscillates fast and greatly. It is attributed to the poor modeling ability for essentially fractional-order systems. In Fig. 7, the real trajectories $x(t)$ s and the target trajectories $r(t)$ s of FOASMC-2, FOASMC-custom with and without constraints are plotted. The results show that the overshoot of FOASMC-2 is small ($< 5\%$), and the trajectory has no oscillation. The overshoot of FOASMC-custom is negligible ($\approx 0.1\%$), and the trajectory has no oscillation. For the FOASMC-custom with $\hat{b} = 1$ and the input constraint imposed, the overshoot is also negligible ($\approx 0.1\%$) and the trajectory has no oscillation.

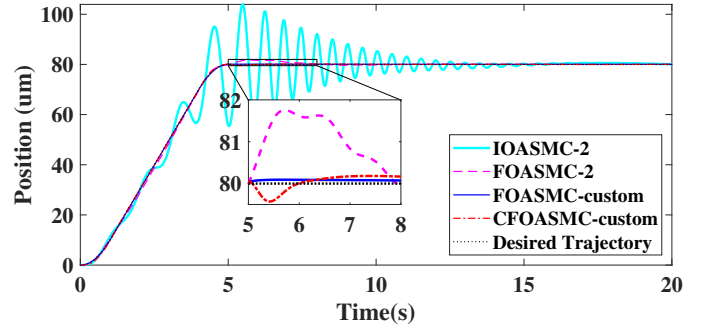


Fig. 7. Trajectories of IOASMC-2, FOASMC-2 and FOASMC-custom.

Remark 5. From the simulation results, it is observed that fractional-order controllers do have superiorities over integer-order controllers. With smaller overshoot and shorter settling time, they perform well even with b unknown, as long as the sign of b is determined. Because of the poor modeling ability of the integer-order models, the corresponding controllers get large overshoot and great oscillation.

B. Experiments

The micromanipulation system is similar to that mentioned in [9]. As shown in Fig. 8, the system consists of an inverted optical microscope (Olympus, IX-53) with a motorized X-Y stage. A camera (Basler, acA640-120gm) is connected to the microscope for visual feedback. On the left side of the microscope, a micromanipulator (Sutter Instrument, MP285A) is mounted on the anti-vibration table to manipulate the holding micropipette. On the right side of the microscope, another micromanipulator (Scientifica, PatchStar) is mounted to manipulate the injection micropipette. A holding micropipette is connected to a syringe, controlled by a stepper motor. An injection micropipette is connected to a pump (Eppendorf, CellTram® 4r Air) controlled by a motor (Tamagawa, TBL-II).

After holding the oocyte, the injection micropipette is manipulated to penetrate the oocyte. Then the gas pressure in the injection micropipette is adjusted by adjusting the motor velocity as equation (19). The enucleation operation is completed by a C++ program totally. Instead of directly controlling the pressure which is approximately linear to the syringe motor position, we control the motor velocity at a frequency of 20 Hz.

IOASMC-2, FOASMC-custom and a PID controller are tested. The parameters of IOASMC-2 and FOASMC-custom are listed in TABLE I. For all controllers, system input $u(t)$ s are constrained to between u_m and u_M . For the PID controller, $k_p = 0.01$, $k_i = 0.0001$, $k_d = 0.15$. The sampling time is 0.05 s. The detection of the interface position in the experiment is not accurate, so if $r(t)$ is set close to 0 in the beginning, the sign of e changes dramatically. Additionally, due to high viscosity, the interface position remains at zero until the pressure reaches the threshold. Therefore, in each experiment, $r(t)$ is set as a constant, which is determined by the sizes of the oocytes and micropipette.

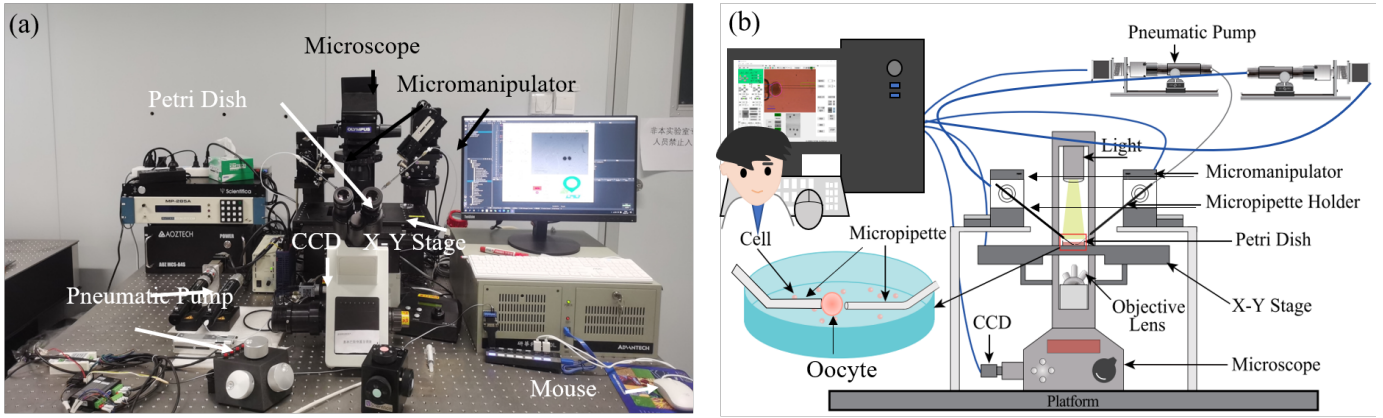


Fig. 8. Robotic SCNT system. (1) inverted microscope; (2) motorized stage; (3) camera; (4) micromanipulator (Sutter Instrument, MP285A); (5) micromanipulator (Scientifica, PatchStar); (6) syringe for holding oocyte; (7) motorized pump;

With given negative pressure, a certain amount of material in the oocyte is aspirated into the micropipette. In the enucleation process, as long as the interface position arrives at the target position, the micropipette withdraws from the oocyte and the enucleation process is finished. But in order to test the steady state performance, the command of withdrawing the micropipette is emitted by the operator with a click of the corresponding button in the user interface.

Extensive experiments are carried out to compare the FOASMC with IOASMC and traditional PID controller. **TABLE II** shows the performance of each controller. The ‘arrival time’ is the first time when the interface arrives at the target position. High velocity during the withdrawal of the micropipette causes more loss than expected, which should be avoided. The RMSE is the root mean square error between $r(t)$ and $y(t)$. In some experiments, the interface position does not change after a long time (one minute) or the pressure increases so that the oocyte is destroyed, which is considered a failure. The target positions are normalized and the corresponding trajectories for these controllers are illustrated in **Fig. 9**. The results indicate that FOASMC is superior to IOASMC and PID controller, with shorter arrival time, less arrival velocity, less RMSE value and the highest success rate. PID controller takes a much longer time, which may be attributed to high diversity of oocytes. Due to bad fitting ability, the IOASMC gets the lowest success rate.

To further compare the efficiency of IOASMC and FOASMC in oocyte development, three groups of oocytes were enucleated with IOASMC and FOASMC successfully and cultured to the cleavage stage.

TABLE III lists the cleavage rate of IOASMC and FOASMC after the enucleation. The IOASMC gets the cleavage rate of 38.04%, while the FOASMC gets a significantly higher cleavage rate of 49.45%. These experiments demonstrate the superiority of the proposed fractional-order sliding mode controller.

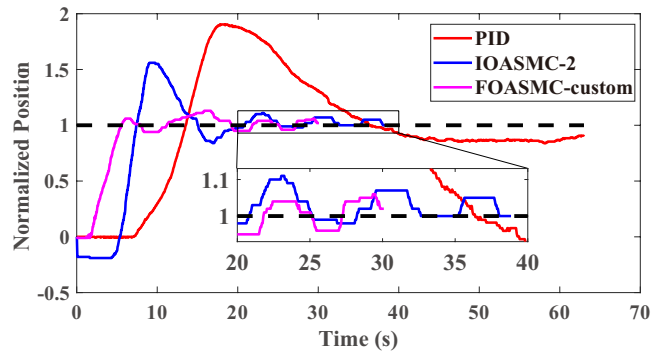


Fig. 9. Trajectories in the experiment. For different controllers, the target positions are different. They are normalized in this figure.

TABLE II
PERFORMANCE COMPARISON OF FOASMC, IOASMC AND PID

Average value	FOASMC	IOASMC	PID
Arrival time	5.01 s	8.37 s	18.72 s
Arrival velocity	92.14 $\mu\text{m/s}$	158.78 $\mu\text{m/s}$	106.05 $\mu\text{m/s}$
RMSE	109.95	186.57	164.61
Success Rate	67/67=100%	29/49=59.18%	56/62=90.32%

V. CONCLUSION

Oocyte enucleation with the micropipette is an important and difficult problem due to its complicated viscoelastic property, significant uncertainty and disturbance. This article identifies fractional-order models of the micropipette enucleation process based on experimental data. These models demonstrate

TABLE III
CLEAVAGE RATE AFTER ENUCLEATION WITH IOASMC AND FOASMC

Group	IOASMC	FOASMC
1	8/30=26.67%	12/29=41.38%
2	18/31=58.04%	21/32=65.63%
3	9/31=29.03%	12/30=40.00%
Average	35/92=38.04%	45/91=49.45%

superior performance compared to integer-order models with the same number of tunable parameters. Based on the identified model, an adaptive sliding mode controller is developed for the incommensurate fractional-order system. FOASMC and IOASMC are simulated and compared with each other. With the same tunable parameters, FOASMC exhibits great superiority over IOASMC. IOASMC has a large overshoot ($> 25\%$) and oscillates fast and greatly, while FOASMC has a slight overshoot ($< 5\%$) and no oscillation is displayed. Experiments on the self-developed micromanipulation system show that the proposed incommensurate fractional-order sliding mode controller is faster and more accurate than integer-order controller and traditional PID controller. The highest success rate and cleavage rate of FOASMC also demonstrate the value of application on somatic cell nuclear transfer.

There are still some limitations of this work. The model is identified based on the collected data, so the physical parameters cannot be integrated into the model directly. In addition, the constraint of the control input is not considered in the controller design section, which may degrade the performance of the controller. In addition, only the parallel fractional Kelvin–Voigt model is considered and a more generalized model [39] could be further adopted.

VI. APPENDIX

Proof of Lemma 2. Taking the Laplace transform of $\mathcal{D}^{\alpha} \mathbf{x}(t) = \mathbf{A}\mathbf{x}(t) + \dot{\mathbf{v}}(t)$ gives

$$\left\{ \begin{array}{l} s^{\alpha_1} X_1(s) - s^{\alpha_1-1} x_1(0) = \sum_{j=1}^n a_{1j} X_j(s) + sV_1(s) \\ \quad - v_1(0), \\ s^{\alpha_2} X_2(s) - s^{\alpha_2-1} x_2(0) = \sum_{j=1}^n a_{2j} X_j(s) + sV_2(s) \\ \quad - v_2(0), \\ \dots \\ s^{\alpha_n} X_n(s) - s^{\alpha_n-1} x_n(0) = \sum_{j=1}^n a_{nj} X_j(s) + sV_n(s) \\ \quad - v_n(0). \end{array} \right. \quad (28)$$

where $X_i(s)$ and $V_i(s)$ are the Laplace transform of $x_i(t)$ and $v_i(t)$, $i = 1, 2, \dots, n$. Equation 28 can be rewritten as

$$\Delta(s) \cdot \begin{pmatrix} X_1(s) \\ X_2(s) \\ \vdots \\ X_n(s) \end{pmatrix} = \begin{pmatrix} b_1(s) \\ b_2(s) \\ \vdots \\ b_n(s) \end{pmatrix}, \quad (29)$$

in which

$$\left\{ \begin{array}{l} b_1(s) = s^{\alpha_1-1} x_1(0) + sV_1(s) - v_1(0) \\ b_2(s) = s^{\alpha_2-1} x_2(0) + sV_2(s) - v_2(0) \\ \dots \\ b_n(s) = s^{\alpha_n-1} x_n(0) + sV_n(s) - v_n(0), \end{array} \right. \quad (30)$$

$$\Delta(s) = \begin{pmatrix} s^{\alpha_1} - a_{11} & -a_{12} & \dots & -a_{1n} \\ -a_{21} & s^{\alpha_2} - a_{22} & \dots & -a_{2n} \\ \vdots & \vdots & \ddots & \vdots \\ -a_{n1} & -a_{n2} & \dots & s^{\alpha_n} - a_{nn} \end{pmatrix}. \quad (31)$$

Multiplying s on both sides of Equation 29 gives

$$\Delta(s) \cdot \begin{pmatrix} sX_1(s) \\ sX_2(s) \\ \vdots \\ sX_n(s) \end{pmatrix} = \begin{pmatrix} sb_1(s) \\ sb_2(s) \\ \vdots \\ sb_n(s) \end{pmatrix}. \quad (32)$$

Based on the final-value theorem of the Laplace transform, we have

$$\lim_{s \rightarrow 0, \text{Re}(s) \geq 0} sV_i(s) = \lim_{t \rightarrow +\infty} v_i(t) = 0. \quad (33)$$

If all roots of the equation $\det(\Delta(s)) = 0$ lie in the open left half complex plane, i.e., $\text{Re}(s) < 0$, then we consider Equation (32) in $\text{Re}(s) \geq 0$. In this restricted area, we have

$$\lim_{s \rightarrow 0, \text{Re}(s) \geq 0} sb_i(s) = \lim_{s \rightarrow 0, \text{Re}(s) \geq 0} (s^{\alpha_i} x_i(0) + s^2 V_i(s) - s v_i(0)) = 0, \quad (34)$$

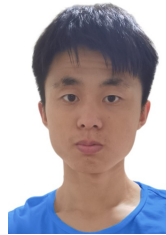
where $i = 1, 2, \dots, n$. $\Delta(s)$ has full rank in $\text{Re}(s) \geq 0$. Therefore, the unique solution $sX_i(s)$, $i = 1, 2, \dots, n$ exists in this area, and we have

$$\lim_{t \rightarrow +\infty} x_i(t) = \lim_{s \rightarrow 0, \text{Re}(s) \geq 0} sX_i(s) = 0. \quad \square$$

REFERENCES

- [1] K. H. S. Campbell, J. McWhir, W. A. Ritchie, and I. Wilmut, "Sheep cloned by nuclear transfer from a cultured cell line," *Nature*, vol. 380, no. 6569, pp. 64–66, Mar. 1996.
- [2] S. Mondal and R. L. Singh, Eds., *Emerging Issues in Climate Smart Livestock Production: Biological Tools and Techniques*. London: Academic Press, 2021.
- [3] H. Niemann and C. Wrenzycki, Eds., *Animal Biotechnology*, vol. 2. Cham: Springer, 2018.
- [4] C. L. Mummery and B. A. J. Roelen, "Cloning human embryos," *Nature*, vol. 498, no. 7453, pp. 174–175, Jun. 2013.
- [5] M. Tigre Moura, Ed., *Somatic Cell Nuclear Transfer Technology*, ser. Methods in Molecular Biology, vol. 2647. New York, USA: Humana, 2023.
- [6] H. Ma *et al.*, "Abnormalities in human pluripotent cells due to reprogramming mechanisms," *Nature*, vol. 511, no. 7508, pp. 177–183, Jul. 2014.
- [7] Z. Liu *et al.*, "Cloning of macaque monkeys by somatic cell nuclear transfer," *Cell*, vol. 172, no. 4, pp. 881–887.e7, Feb. 2018.
- [8] J. Zhai *et al.*, "Neurulation of the cynomolgus monkey embryo achieved from 3D blastocyst culture," *Cell*, vol. 186, no. 10, pp. 2078–2091.e18, May. 2023.
- [9] M.-Z. Sun *et al.*, "Intracellular strain evaluation-based oocyte enucleation and its application in robotic cloning," *Engineering*, Jun. 2022.
- [10] Q. Zhao *et al.*, "Robotic cell rotation based on the minimum rotation force," *IEEE Trans. Autom. Sci. Eng.*, vol. 12, no. 4, pp. 1504–1515, Oct. 2015.
- [11] Y. Liu *et al.*, "Oocyte orientation selection method based on the minimum strain position in the penetration process," *J. Appl. Phys.*, vol. 125, no. 15, p. 154701, Apr. 2019.
- [12] Y. Liu *et al.*, "Oocyte penetration speed optimization based on intracellular strain," *Micromachines*, vol. 13, no. 2, p. 309, Feb. 2022.

- [13] X. P. Zhang, C. Leung, Z. Lu, N. Esfandiari, R. F. Casper, and Y. Sun, "Controlled aspiration and positioning of biological cells in a micropipette," *IEEE Trans. Biomed. Eng.*, vol. 59, no. 4, pp. 1032–1040, Apr. 2012.
- [14] Z. Zhang *et al.*, "Robotic pick-and-place of multiple embryos for vitrification," *IEEE Robot. Autom. Lett.*, vol. 2, no. 2, pp. 570–576, Apr. 2017.
- [15] X. Zhao *et al.*, "Aspirating cell into orifice of micropipette for precise cell transportation using micropipette," *IEEE Trans. Autom. Sci. Eng.*, pp. 1–11, 2022.
- [16] G. Shan *et al.*, "Robotic blastocyst biopsy," *IEEE/ASME Trans. Mechatron.*, vol. 28, no. 3, pp. 1372–1383, Jun. 2023.
- [17] M. Sun *et al.*, "Precise aspiration and positioning control based on dynamic model *inside* and *outside* the micropipette," *IEEE Trans. Autom. Sci. Eng.*, vol. 20, no. 1, pp. 385–393, Jan. 2023.
- [18] Y. Liu *et al.*, "A Cell's Viscoelasticity Measurement Method Based on the Spheroidization Process of Non-Spherical Shaped Cell," *Sensors*, vol. 21, no. 16, p. 5561, Jan. 2021.
- [19] C. Ma and Y. Hori, "Fractional-order control: theory and applications in motion control [past and present]," *IEEE Ind. Electron. Mag.*, vol. 1, no. 4, pp. 6–16, 2007.
- [20] I. Podlubny, *Fractional Differential Equations*. New York, NY, USA: Academic Press, 1999.
- [21] M. Zhou, H. Su, Y. Feng, K. Wei, W. Xu, and J. Cheng, "Super-twisting algorithm-based fractional -order sliding-mode control of nonlinear systems with mismatched uncertainties," *IEEE Trans. Ind. Electron.*, vol. 71, no. 8, pp. 9510–9519, 2024.
- [22] P. Perdikaris and G. E. Karniadakis, "Fractional-order viscoelasticity in one-dimensional blood flow models," *Ann. Biomed. Eng.*, vol. 42, no. 5, pp. 1012–1023, May. 2014.
- [23] J. Wang, Y. Ni, X. Zhang, Z. Li, C. Wang, and C.-Y. Su, "Adaptive neural indirect inverse control for a class of fractional-order hysteretic nonlinear time-delay systems and its application," *IEEE Trans. Ind. Electron.*, pp. 1–11, 2024.
- [24] J. Wu, Z. Xu, Y. Zhang, C. Su, and Y. Wang, "Modeling and tracking control of dielectric elastomer actuators based on fractional calculus," *ISA Trans.*, vol. 138, pp. 687–695, Jul. 2023.
- [25] P. Gong and W. Lan, "Adaptive robust tracking control for multiple unknown fractional-order nonlinear systems," *IEEE Trans. Cybern.*, vol. 49, no. 4, pp. 1365–1376, 2019.
- [26] Y.-C. Fung, *Biomechanics*. New York, USA: Springer, 1993.
- [27] A. Gemant, "A method of analyzing experimental results obtained from elasto-viscous bodies," *J. Appl. Phys.*, vol. 7, no. 8, pp. 311–317, Dec. 2004.
- [28] R. L. Bagley and P. J. Torvik, "A theoretical basis for the application of fractional calculus to viscoelasticity," *J. Rheol.*, vol. 27, no. 3, pp. 201–210, Jun. 1983.
- [29] X. Zhao, M. Cui, Y. Zhang, Y. Liu, and X. Zhao, "Robotic precisely oocyte blind enucleation method," *Appl. Sci.*, vol. 11, no. 4, p. 1850, Jan. 2021.
- [30] G. Sun, L. Wu, Z. Kuang, Z. Ma, and J. Liu, "Practical tracking control of linear motor via fractional-order sliding mode," *Automatica*, vol. 94, pp. 221–235, 2018.
- [31] M. Vahdanipour and M. Khodabandeh, "Adaptive fractional order sliding mode control for a quadrotor with a varying load," *Aerosp. Sci. Technol.*, vol. 86, pp. 737–747, 2019.
- [32] C. Hua, J. Chen, and X. Guan, "Fractional-order sliding mode control of uncertain QAVs with time-varying state constraints," *Nonlinear Dyn.*, vol. 95, no. 2, pp. 1347–1360, 2019.
- [33] X. Li, J. He, C. Wen, and X.-K. Liu, "Backstepping-based adaptive control of a class of uncertain incommensurate fractional-order nonlinear systems with external disturbance," *IEEE Trans. Ind. Electron.*, vol. 69, no. 4, pp. 4087–4095, Apr. 2022.
- [34] S. Song, J. H. Park, B. Zhang, and X. Song, "Observer-based adaptive hybrid fuzzy resilient control for fractional-order nonlinear systems with time-varying delays and actuator failures," *IEEE Trans. Fuzzy Syst.*, vol. 29, no. 3, pp. 471–485, Mar. 2021.
- [35] X. Wang *et al.*, "Effect of cell inner pressure on deposition volume in microinjection," *Langmuir*, vol. 34, no. 35, pp. 10287–10292, Sep. 2018.
- [36] Q. Zhao *et al.*, "A novel pneumatic micropipette aspiration using a balance pressure model," *Rev. Sci. Instrum.*, vol. 84, no. 12, p. 123703, Dec. 2013.
- [37] H. Xu and X. Jiang, "Creep constitutive models for viscoelastic materials based on fractional derivatives," *Comput. Math. Appl.*, vol. 73, no. 6, pp. 1377–1384, Mar. 2017.
- [38] M. Caputo, "Linear models of dissipation whose Q is almost frequency independent—II," *Geophys. J. Int.*, vol. 13, no. 5, pp. 529–539, Nov. 1967.
- [39] R. Hilfer, *Applications of Fractional Calculus in Physics*. Singapore: World Scientific, 2000.
- [40] Y. Chen, I. Petras, and D. Xue, "Fractional order control - a tutorial," in *Proc. 2009 American Control Conf.*, pp. 1397–1411, Jun. 2009.
- [41] T. Abdeljawad, "On Riemann and Caputo fractional differences," *Comput. Math. Appl.*, vol. 62, no. 3, pp. 1602–1611, Aug. 2011.
- [42] A. Tepljakov, "FOMCON toolbox for matlab," 2024. [Online]. Available: <https://www.mathworks.com/matlabcentral/fileexchange/66323-fomcon-toolbox-for-matlab>
- [43] T. F. Coleman and Y. Li, "An interior trust region approach for nonlinear minimization subject to bounds," *SIAM J. Optim.*, vol. 6, no. 2, pp. 418–445, May. 1996.
- [44] C. Huang, J. Gao, S. Mo, and J. Cao, "Hopf bifurcation in a fractional-order neural network with self-connection delay," *Nonlinear Dyn.*, vol. 111, pp. 14335–14350, Jun. 2023.
- [45] F. Luan, J. Na, Y. Huang, and G. Gao, "Adaptive neural network control for robotic manipulators with guaranteed finite-time convergence," *Neurocomputing*, vol. 337, pp. 153–164, Apr. 2019.



Yujie Zhang received the B.S. degree in intelligent science and technology from Nankai University, Tianjin, China, in 2020. He is currently pursuing the Ph.D degree in control science and engineering at Nankai University. His research interests include micromanipulation and control theory.



Bingxin Li received the B.S. degree in automation from Shandong University, Jinan, China, in 2014, and the M.S. degree in systems analysis and integration from Northeastern University, Shenyang, China, in 2017. He is currently pursuing the Ph.D. degree in control science and engineering at Nankai University. His research interests include fractional order control systems, singular systems, and robust control.



Yaowei Liu received the B.Eng. degree in automation and the Ph.D. degree in control theory and control engineering from Nankai University, Tianjin, China, in 2013 and 2019, respectively. He was a Postdoctoral Researcher with the College of Artificial Intelligence, Nankai University, in 2023, where he is currently an Assistant Professor. His research interests include robotic cell micromanipulation and robotic cell measurement.



Xin Zhao received the B.S. degree in control theory and control engineering from Nankai University, Tianjin, China, in 1991, the M.S. degree in control theory and control engineering from the Shenyang Institute of Automation, CAS, Shenyang, China, in 1994, and the Ph.D. degree in control theory and control engineering from Nankai University, in 1997. He joined as a Faculty Member with Nankai University, in 1997, where he is currently a Professor and the Dean of the College of Artificial Intelligence. He is also with the Institute of Intelligence Technology and Robotic Systems, Shenzhen Research Institute of Nankai University, Shenzhen, China. His research interests include micromanipulators, microsystems, and mathematical biology.